Nanoscale kinetics and dynamics during Ar^{+} patterning of SiO_{2}

Mahsa Mokhtarzadeh, Jeffrey G. Ulbrandt, Peco Myint, Suresh Narayanan, Randall L. Headrick, and Karl F. Ludwig, Jr.

Nanoscale Kinetics and Dynamics during Ar$^+$ Patterning of SiO$_2$

Mahsa Mokhtarzadeh[1,2], Jeffrey G. Ulbrandt[3], Peco Myint[4],
Suresh Narayanan[5], Randall L. Headrick[3], Karl F. Ludwig, Jr.[1,4*]

[1]*Department of Physics, Boston University, Boston, Massachusetts 02215 USA*
[2]*Department of Physics, Shahid Beheshti University, Tehran, Iran*
[3]*Department of Physics and Materials Science Program, University of Vermont, Burlington, Vermont 05405 USA*
[4]*Division of Materials Science and Engineering, Boston University, Boston, Massachusetts 02215 USA and*
[5]*Advanced Photon Source, Argonne National Lab, Argonne, IL, 60439 USA*

Broad-beam low-energy ion bombardment can lead to the spontaneous formation of nanoscale surface structures, but the dominant mechanisms driving evolution remain controversial. Using coherent x-ray scattering to examine the classic case of ion beam rippling of SiO$_2$ surfaces, we study the relationship between the average kinetics of ripple formation and the underlying fluctuation dynamics. The early stage growth of fluctuations is well fit with a linear theory formalism employing a viscous relaxation term with full wavenumber dependence. In this regime, the x-ray photon correlation spectroscopy (XPCS) two-time correlation function shows novel behavior, with memory stretching back to the beginning of the bombardment. For a given length scale, correlation times do not grow significantly beyond the characteristic time associated with the early-stage ripple growth. In the late stages of patterning, when the average surface structure on a given length scale is no longer evolving, dynamical processes continue on the surface. Nonlinear processes dominate at long length-scales, leading to compressed exponential decay of the speckle correlation functions, while at short length-scales the dynamics appears to approach a linear behavior consistent with viscous flow relaxation. This behavior is found to be consistent with simulations of the anisotropic Kuramoto-Sivashinsky equation. In addition, it is shown that the surface ripple velocity, an important parameter of the ion-driven surface evolution, can be measured with coherent x-ray scattering in conjunction with use of an inhomogeneous ion beam. The change in viewpoint exemplified by this study, from a focus on only average surface kinetics to one incorporating the underlying nanoscale dynamics, is rapidly becoming more widely applicable as new and upgraded x-ray sources with higher coherent flux come online.

Hyperthermal ion and atom beams are ubiquitous in surface science and technology. In addition to plasma etching and surface passivation, common processes employing hyperthermal beams include sputter etching, sputter deposition, ion beam assisted deposition and a variety of plasma-enhanced growth techniques. Moreover, depending upon materials properties and irradiation conditions, broad-beam low-energy ion bombardment can lead to the spontaneous formation of nanoscale surface structures, such as ripples[1] and dots[2], or instead to the ultra-smoothening of surfaces[3]. This has the potential of being useful for inexpensive large-scale patterning. However, fundamental questions remain about the dominant processes driving spontaneous ion beam nanopatterning in a given situation[1,4−10].

Understanding the interplay between nanoscale kinetics and dynamics on the self-organizing surface is an essential task, though one not often explicitly attempted. By "kinetics", we mean the evolution of the average nanoscale surface structure, which can be powerfully investigated in real time by "non-coherent" x-ray scattering in a surface sensitive mode. By "dynamics" we mean the evolution of fluctuations about the average, which occurs not only on the atomic scale but on the nanoscale as well. The difference between the two is perhaps most obvious in thinking about the late stage of many surface growth and modification processes in which the surface reaches a dynamic steady state, so that there is no longer an average kinetic evolution. However surface processes of ion impact or atom arrival and diffusion continue so that there is still ongoing dynamics. Investigating these dynamics has become possible using surface-sensitive coherent x-ray scattering, though as yet, the limited coherent x-ray flux available and the challenge of integrating *in-situ* surface equipment into an appropriate synchrotron x-ray beamline have limited the number of existing experiments[11−15]. In particular, x-ray photon correlation spectroscopy (XPCS) uses correlations of the scattering speckle pattern to investigate the dynamics of fluctuations[16,17].

Here we use surface-sensitive coherent x-ray scattering to investigate the classic case of ion beam nanoscale rippling of an SiO$_2$ surface[18,19]. Analyzing the speckle-averaged scattering provides information about the average kinetic evolution of the surface during ripple formation while analyzing speckle correlations, and even the speckle motion itself, gives insight into the underlying dynamics. Both come from the same data set, providing a clear view of how the kinetics and dynamics evolve together.
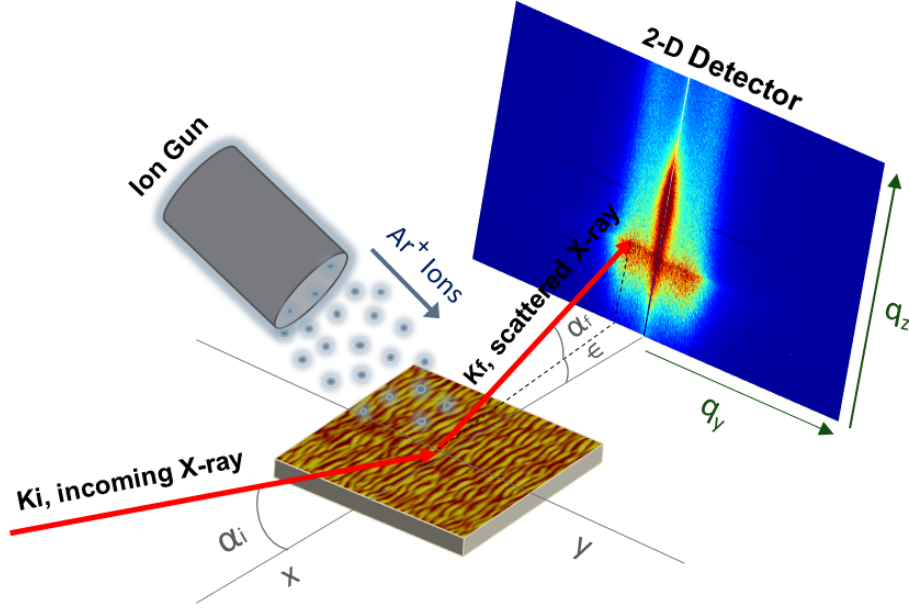
FIG. 1: Schematic diagram of coherent small-angle x-ray scattering (Co-GISAXS) measurements during Ar^+ ion bombardment of SiO_2. The sample is inclined by a small angle α_i with respect to the incoming X-ray beam and the diffuse scattering is recorded as a function of the exit angles α_f and ψ using a 2D detector.

I. METHODS

Samples were 1000 nm wet thermal oxide on p-doped(B) Si(100) with resistivity 1-100 $\Omega \cdot$cm, affixed to a molybdenum sample platen with silver paste. The entire area of the sample platen was covered with Si to minimize secondary collisions that can lead to sputtering of impurities onto the surface. The sample platen was mounted in a custom vacuum chamber with base pressure 1×10^{-8} Torr. Samples were bombarded with 2 keV Ar^+ ions at angles of either 45° or 65° at room temperature. These are conditions that lead to the spontaneous formation of nano-ripple patterns. The ion beam was generated by an RBD Instruments 04-165 Sputter Ion Gun with multiple focus settings. The ion flux was in the range of $5 \times 10^{13} - 3 \times 10^{14} \frac{\text{ions}}{\text{cm}^2 \cdot \text{sec}}$ depending on the ion beam focus position. The 45 °data were taken with both an unfocused and a focused ion beam (focus position 4 - highly focused) and the 65 degree data were taken with focus position 2.5 (less focused).

The coherent x-ray scattering studies were performed at sector 8-ID-I of the Advanced Photon Source at Argonne National Laboratory. The photon energy of 10.9 keV (0.114 nm wavelength) was selected by a Ge(111) monochromator with a resulting flux of approximately 1×10^{10} photons/s and beam dimensions $0.02\,\text{mm} \times 0.02\,\text{mm}$. Experiments used an X-Spectrum Lambda detector with 1536 x 512 pixels 55 μm in size and located 3.93 m from the sample.

Figure 1 depicts the grazing-incidence small-angle x-ray scattering (GISAXS) geometry. The sample is inclined by a small angle α_i with respect to the incoming X-ray beam and the diffuse scattering is recorded as a function of the exit angles α_f and ψ using a 1536×512 pixel Lambda X-ray detector. The X-ray measurements were performed with an incidence angle $\alpha_i = 0.24°$ and with projected incident x-ray beam direction perpendicular to the ion beam direction (i.e., revealing corrugations with wavevector parallel to the ion beam).

Figure 2 displays an example of a GISAXS scattering pattern. At both ion incidence angles investigated, the GISAXS evolution is qualitatively similar, with an early time peak growth that shifts in to lower $q_{||}$ values.The analysis presented in the manuscript is for data at the Yoneda wing position for which α_f is equal to the critical angle. Both the vertical and horizontal axis on the detector image include q_x components; however, since $q_x \ll q_y$ and $q_x \ll q_z$ as a result of the small incidence and exit angles, and because the surfaces are isotropic, the horizontal axis $q_{||}$ (parallel to the surface) can be approximated as simply q_y and the vertical axis can be considered as q_z (perpendicular to the surface). When there is no danger of confusion, we will simply refer to q_y as q.
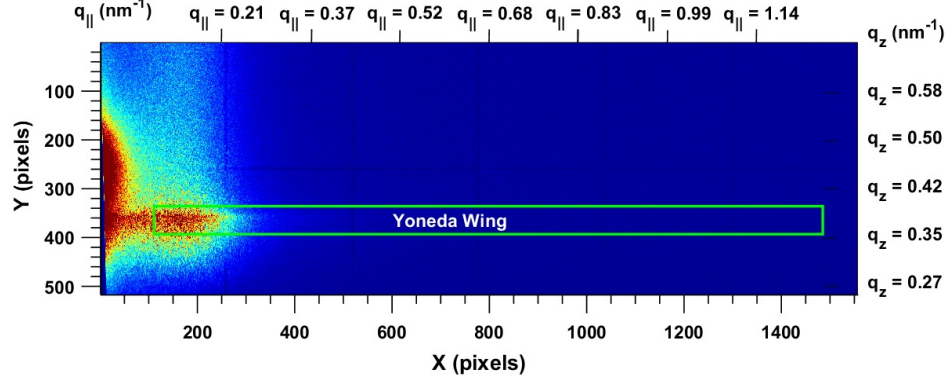
FIG. 2: Example x-ray detector image recorded during beam nanopatterning. The Yoneda wing is the surface-sensitive scattering exiting the sample at the critical angle. The Yoneda wing intensity centered at X-position of approximately 150 pixels is due to the growth of correlated nanoripples on the surface. The intensity at lowest X-position is due to long wavelength surface roughness. The components of the wavevector transfer $\boldsymbol{q}$ have been written on the detector image.

II. OVERALL BEHAVIOR

XPCS experiments use an x-ray beam with partial coherence, so that the structural disorder within the illuminated sample volume produces speckle in the x-ray scattering pattern. Averaging over the speckle pattern produces the same information obtained from a real-time "non-coherent" experiment – namely a measure of the average sample structure evolution. Figure 3 shows the general behavior observed for bombardment at 45°; qualitatively similar behavior is also observed for 65° bombardment. In the figure, the speckle-averaged scattered x-ray intensity is shown as a function of the wavenumber q, which is the in-plane component of the wavevector transfer during x-ray scattering. Intensity at a given wavenumber q is closely related to the strength of surface fluctuations at a corresponding length-scale $d = 2\pi/q$.
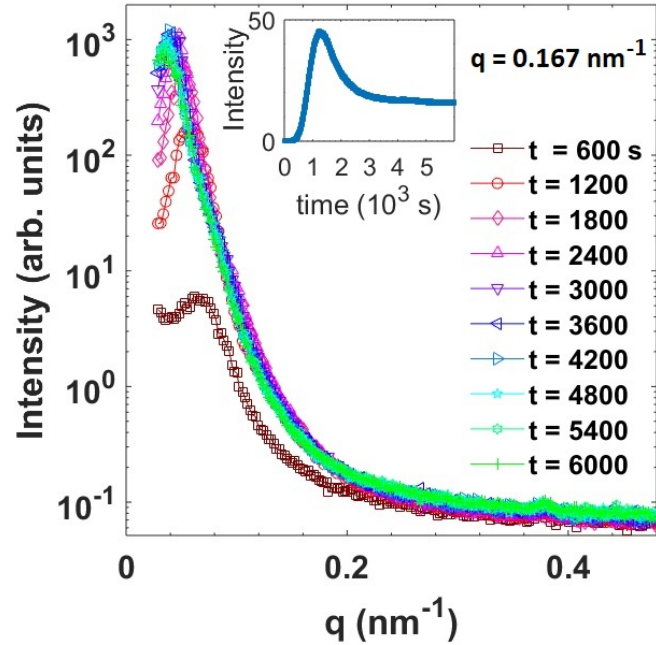

FIG. 3: Averaged x-ray scattering pattern evolution during ion beam nanopatterning at 45° bombardment angle. The inset shows that the averaged intensity at a given wavenumber (reflecting the average surface spatial fluctuations on the corresponding length scale) increases to a maximum and then relaxes to a steady-state value .
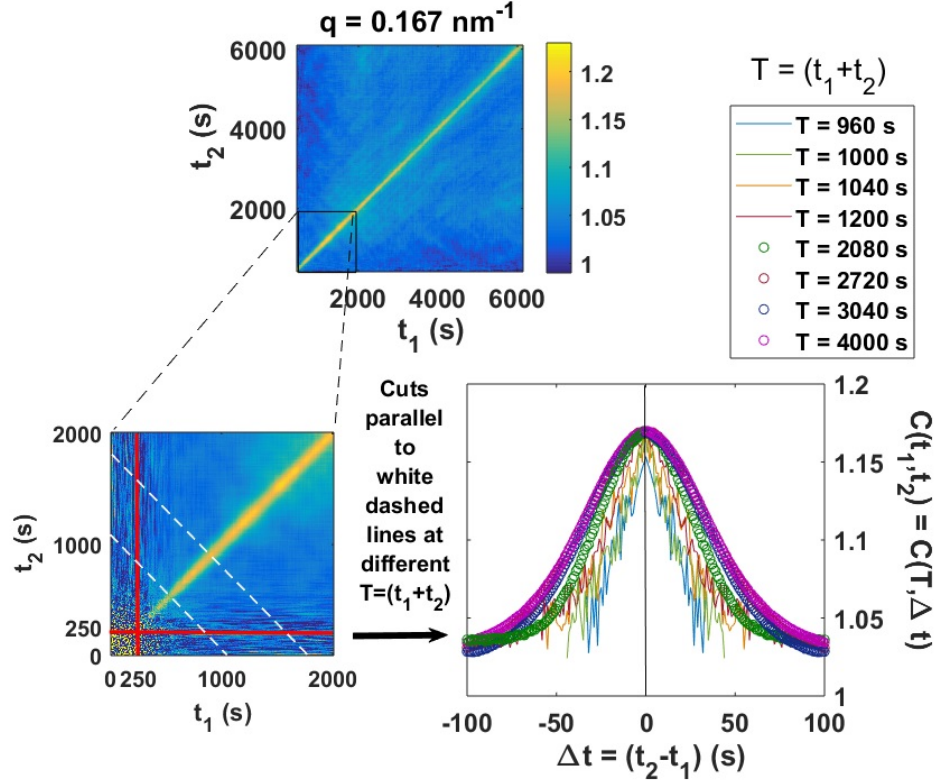
FIG. 4: Evolution of the Two-Time Correlation Function during nanopatterning at 45°. The two-time correlation function (TTCF) shown in the top image measures the extent to which the surface structure has changed between times t_1 and t_2. The width of the central diagonal line $t_1 \approx t_2$ therefore shows the time over which the surface remains correlated during the patterning process. The ion bombardment began at 250 s, marked by red lines on the blow-up shown in the bottom left image. The bottom right image shows perpendicular cuts through the TTCF as the patterning proceeds. The width of the correlation peak increases from the time that bombardment begins (reflecting increasing surface correlation times) but eventually saturates. For comparison purposes in this figure, the heights of the perpendicular cuts are normalized to a constant value.

As seen in Fig. 3, a peak grows in the averaged scattering pattern; this is due to the formation of correlated ripples on the surface with an initial wavelength of approximately $2\pi/q_{initial} \approx 2\pi/0.17$ nm^{-1} ≈ 37 nm. With time, the peak shifts to lower wavenumbers showing that the average wavelength coarsens. As shown in the inset of Fig. 3, for medium- and high-wavenumbers, the intensity reaches a maximum and decreases to a steady state.

While the evolving speckle-averaged x-ray scattering pattern reveals the average patterning kinetics, in XPCS experiments temporal correlation functions of the detailed speckle patterns themselves are used to probe fluctuations about the average – the underlying dynamics itself. The two-time correlation function (TTCF) $C(q, t_1, t_2)$:

$$C(q, t_1, t_2) = \frac{\langle I(q, t_1)I(q, t_2)\rangle}{\langle I(q, t_1)\rangle \langle I(q, t_2)\rangle} \tag{1}$$

measures how structure on a given length-scale changes between time t_1 and time t_2 as the sample evolves. Here the angular brackets denote an average over equivalent q values. Figure 4 shows the TTCF at $q = 0.167$ nm^{-1}. The central diagonal ridge of correlation going from the bottom left to top right of the upper and left heat-maps correspond to the high correlation expected for $t_1 \approx t_2$. One way to evaluate how long it takes for the surface to change configuration on a given length-scale as nanopatterning proceeds is to examine the width of this central ridge by taking cuts through it, as shown by the white dashed lines in the figure. The bottom right hand plot of of Fig. 4 shows such cuts for different values of the total time $T = (t_1 + t_2)$. As can be seen, the width of the correlation function increases during the early stages of bombardment, indicative of growing correlation times, and then reaches a steady state.

Figure 5 displays an AFM topograph taken after approximately 6000 seconds of bombardment at 45°. Well-defined ripples with 10-15 nm of amplitude and 75-100 nm of wavelength form on the surface. This is consistent with the
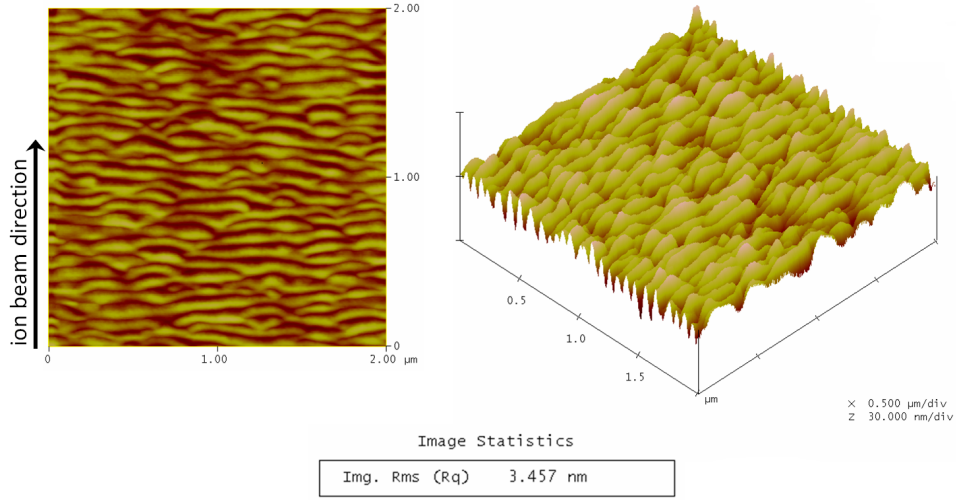
FIG. 5: AFM topograph of the surface after 6000 s of bombardment at irradiation angle of 45°.

earlier study of Umbach *et al.*[18]. The more recent studies of Kumar *et al.*[19] and Keller *et al.*[20] used ion energies of 200-1000 eV, below the 2000 eV energy used here. However, extrapolating ripple wavelength values from their data suggests that they are also consistent with the present results.

III. EARLY-TIME KINETICS

The goal of most studies of ion-induced pattern formation is to understand the evolution of the surface height $h(\mathbf{r}, t) = h(x, y, t)$. A powerful approach is to focus on early times during pattern development, when the amplitude of fluctuations in the surface height is small. Linear stability theory applied to surface evolution during ion bombardment takes the form[1]:

$$\frac{\partial \tilde{h}\left(\mathbf{q}, t\right)}{\partial t} = R\left(\mathbf{q}\right) \tilde{h}\left(\mathbf{q}, t\right) + \tilde{\eta}\left(\mathbf{q}, t\right) \tag{2}$$

where $\tilde{h}\left(\mathbf{q}, t\right)$ is the Fourier transform of the surface height $h\left(\mathbf{r}, t\right)$, $R\left(\mathbf{q}\right)$ is the *amplification factor* or *dispersion relation* whose sign for a given wavenumber denotes stability or instability at the corresponding length-scale, and $\tilde{\eta}\left(\mathbf{q}, t\right)$ is the Fourier transform of a stochastic noise. The amplification factor can be determined experimentally by measuring the speckle-averaged height-height structure factor evolution[6,21]:

$$I(\mathbf{q}, t) = \left\langle h(\mathbf{q}, t)\, h^*(\mathbf{q}, t) \right\rangle = \left(I_0(\mathbf{q}) + \frac{\eta}{2R(\mathbf{q})}\right) e^{2R(\mathbf{q})t} - \frac{\eta}{2R(\mathbf{q})} \tag{3}$$

where η is the magnitude of the stochastic noise: $\left\langle \eta\left(\mathbf{r}, t\right) \eta\left(\mathbf{r}', t\right) \right\rangle = \eta\, \delta(\mathbf{r} - \mathbf{r}')\delta(t - t')$. The amplification factor contains the essential physics determining surface stability or instability. A positive $R(\mathbf{q})$ at a given bombardment angle drives exponential amplification of modes of wavevector $\mathbf{q}$ leading to topographic instability. Conversely a negative $R(\mathbf{q})$ damps fluctuations and stabilizes modes of wavevector $\mathbf{q}$.

To determine $R(q_x \approx 0, q_y) \equiv R(q_y)$, the intensity values $I(q_y, t)$ at each wavenumber have first been averaged over 10 detector pixels in the q_y direction and 21 pixels in the q_z direction (approximately the width of the Yoneda wing) to remove speckle from the coherent scattering pattern. The temporal evolution of each wavenumber bin was then fit with a function $I(q_y, t) = a + b \cdot exp[2Rt]$, with a, b and R being the fit parameters for each q_y bin (Fig. 6).

Figure 7a displays the resulting fit $R(q_y)$ values for an incidence angle of 45°, and Fig. 7b shows the values for irradiation angle 65°. The fit $R(q_y)$ values can themselves be fit as a function of q_y. Work in the field has usually assumed a generic long-wave form:

$$R(q_y) = -S_y\, q_y^2 - B\, q_y^4 \tag{4}$$

where S_y is a coefficient of curvature-dependent surface evolution and B is a coefficient of surface viscous flow smoothening[1,18]. We have recently shown[21] that grazing-incidence small-angle x-ray scattering (GISAXS) includes
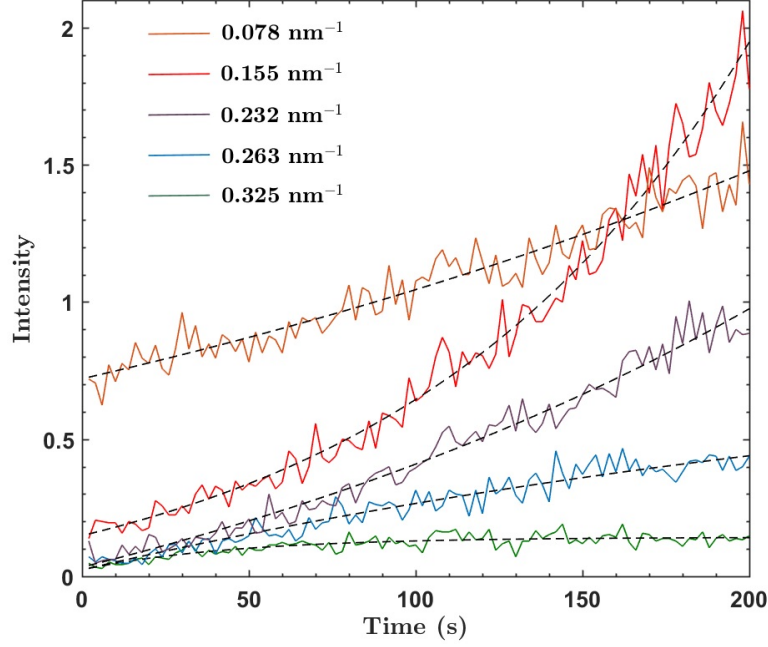
FIG. 6: Early time intensity evolution at different wavenumbers and linear theory fits for irradiation angle 45°.

high-wavenumber information which cannot be fit by the long-wave form of Eq. 4 but instead requires a more detailed model based on the physical processes operating on the surface. The q_y^4 term is a long-wave approximation to the full Orchard solution of viscous flow in a surface layer[22]. Using the full Orchard term gives an amplification factor of the form:

$$R(q_y) = -S_y\, q_y^2 - \frac{\gamma}{2\eta h_0}\left(\frac{Q\left(\sinh(2Q) - 2Q\right)}{1 + 2Q^2 + \cosh(2Q)}\right) \qquad (5)$$

where γ is the surface energy, h_0 is the viscous amorphous layer thickness, $Q = q_y h_0$, and η is the viscosity, which in this case characterizes the ion-enhanced viscous flow (IVF). For the q_y^2 term of Eq. 4, which determines the low-wavenumber stability/instability, there are physical models of erosive-[23] and stress-[9,10] driven patterning that predict a full wavenumber dependence of the term rather than just its low-q limit. We have examined fits of the experimental $R(q)$ data to the predictions of different models and found that the longwave form of Eq. 4 does not well fit the experimental results, particularly for the 45° data set for which $R(q)$ can be fit to a higher wavenumber. Use of the full Orchard term for surface viscous flow, Eq. 5, produces good fits when used with a simple q^2 curvature term or any of the other three terms determining stability. Figure 7 shows both fits using the long-wave form of Eq. 4 and fits using the full Orchard form of Eq. 5. For the 45° data, the fits of the long-wave form to the entire q-range are so poor that we have fit only the $R(q)$ data for $q < 0.21$ nm^{-1} with that model.

For the long-wave fits using Eq. 4, the fit parameters for 45° bombardment are:

$$S_y(45°) = -0.37\,\mathrm{nm^2/s}; \ \ B(45°) = 6.63\,\mathrm{nm^4/s} \implies q_{max} = \sqrt{\frac{|S_y|}{2B}} = 0.168\,\mathrm{nm^{-1}} \qquad (6)$$

and for 65° bombardment are:

$$S_y(65°) = -0.0466\,\mathrm{nm^2/s}; \ \ B(65°) = 0.781\,\mathrm{nm^4/s} \implies q_{max} = \sqrt{\frac{|S_y|}{2B}} = 0.173\,\mathrm{nm^{-1}} \qquad (7)$$

Comparing the ratio of $\frac{|S_y|}{B}$ for the two cases, we conclude that the relative contributions of the terms S_y and B are almost equal for the two bombardment angles. The data at 45° was taken with a more highly focused ion beam compared to the 65°; therefore, the absolute value differences of S_y and B at these two bombardment angles can be largely due to the different values of the ion flux (approximately 3×10^{14} ions/cm^{2}s for the 45° bombardment versus approximately 5×10^{13} ions/cm^{2}s for the 65° data). In linear theory, the fastest growth rate occurs at $q_{max} = \sqrt{\frac{|S_y|}{2B}}$;

the calculated values are consistent with the early time peak positions of the intensity profile. Note that Fig. 3 shows significant coarsening with time as the peak shifts to lower wavenumbers.

For the fits using the Orchard term, we obtain:

$$S_y(45°) = -0.503 \, \text{nm}^2/\text{s}; \; h_0 = 3.4 \, \text{nm}; \; \frac{\gamma}{2\eta_{IVF}h_0} = 2.03 \times 10^{-1} \text{s}^{-1} \tag{8}$$

$$S_y(65°) = -0.0691 \, \text{nm}^2/\text{s}; \; h_0 = 3.1 \, \text{nm}; \; \frac{\gamma}{2\eta_{IVF}h_0} = 3.78 \times 10^{-2} \text{s}^{-1} \tag{9}$$

These detailed results invite comparison with theory and simulation. SRIM simulations[24] give the average penetration depth of 2 keV Ar^+ ions into SiO_2 at 45° and 65° as 3.8 nm and 2.9 nm respectively. Thus the fit values of the the viscous layer thickness h_0 are reasonable.

The amplitude of the Orchard relaxation term is proportional to the ratio γ/η_{IVF}. Literature values of the SiO_2 surface energy γ vary, but are typically in the range of 0.2 J/m^2. This implies values for the ion-enhanced viscosity of $\eta_{IVF} = 1.4 \times 10^8$ Pa·s for the 45° bombardment and 7.8×10^8 Pa·s for the 65° bombardment. There are few numbers in the literature to which these can be compared. In their recent paper, Kumar *et al.*[19] suggest that for 65° bombardment, $\eta_{IVF} = 5 \times 10^{22}$ Pa·ions/cm^2 for 500 eV Ar^+ bombardment of SiO_2. If we use the Kumar *et al.* value without correction for differences in ion energy and incidence angle, it gives predicted values for the present experimental conditions of: $\eta(45°) = 1.7 \times 10^8$ Pa·s and $\eta(65°) = 1 \times 10^9$ Pa·s. Given the many uncertainties in parameters, this is in remarkably good agreement with our experimental fit values.

As noted above, curvature-dependent sputter yield, lateral mass redistribution (often combined within a crater-function approach) and stress could all play a role in determining S_y. Calculation of the erosive contribution to the curvature coefficient is complicated, though, by uncertainties in the sputter yield as a function of ion incidence angle $Y(\theta)$. Seah and Nunney[25] suggest that adding together the sputter yields of Si and O from the SRIM simulation package gives reasonable results at zero bombardment angle. However, Seah *et al.*[26] argue that SRIM considerably overestimates the angular dependence of the Ar^+ sputter yield for low mass targets, and that the angular dependence of Yamamura *et al.*[27] is more accurate. Using SRIM values for $Y(\theta = 0)$, penetration depth and straggle at 45°, coupled with the Yamamura correction to $Y(\theta)$ using known parameters from Si, gives $S_y^{erosive} \sim$ -0.31 nm^2/s. Given the many uncertainties, this must be viewed as quite close to the value of -0.50 nm^2/s obtained from the fit using the Orchard term, which is presumably the most reliable of the two fitting approaches. At 45°, simple models of lateral mass redistribution and stress suggest that they should have no contribution.

At 65°, the erosive contribution to S_y is calculated to be stabilizing, with a magnitude of 0.056 nm^2/s. SRIM collision results can be used to estimate the average total displacement per ion to be approximately $d = 16.0$ nm, giving a lateral mass redistribution contribution to S_y that is destabilizing but smaller in magnitude, with a value of -0.013 nm^2/s. Thus the observed instability to ripple formation at this angle might be driven by stress effects. Simply
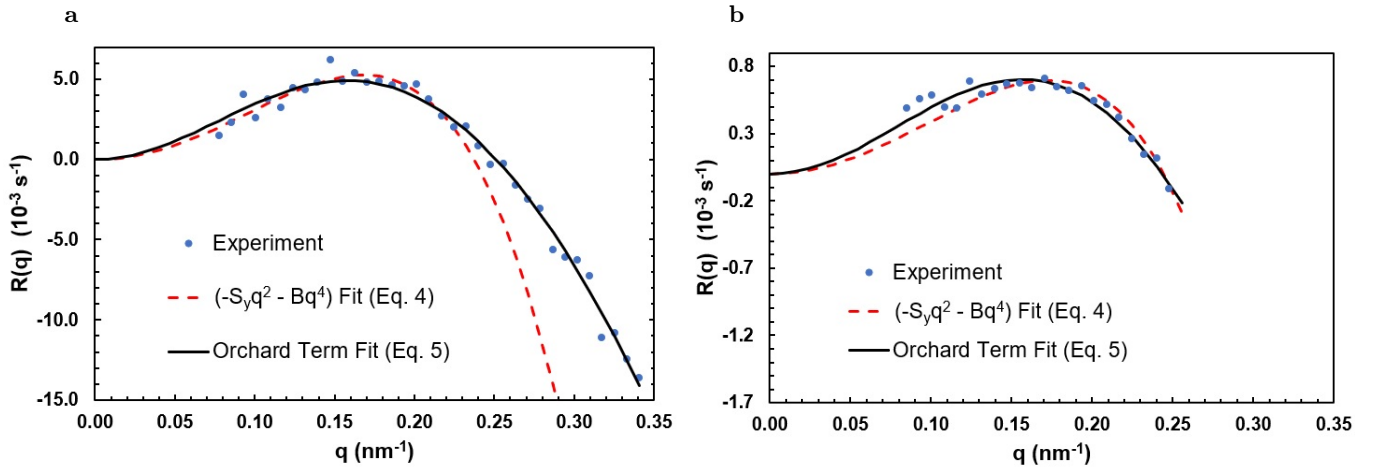

FIG. 7: Linear theory amplification factors with fits. Fits are for low-wavenumber (Eq. 4) and full Orchard term (Eq. 5) forms. a) Irradiation angle 45°. The low-wavenumber ($-S_y q^2 - B q^4$) fit is performed only for data with $q <$ 0.21 nm^{-1}. b) Irradiation angle 65°.
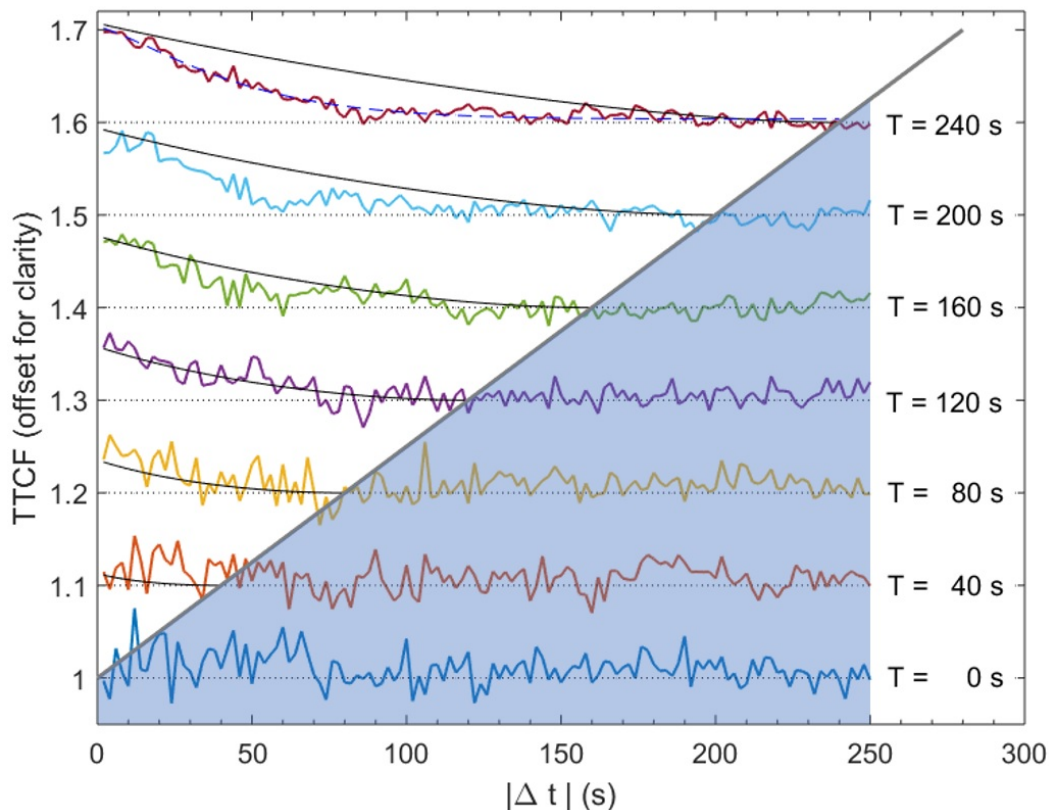
FIG. 8: Novel behavior of the early-time two-time TTCF and comparison with predictions of linear theory. Each succeeding TTCF curve is offset vertically by 0.1 for clarity. The thick diagonal line is the time horizon at which $|\Delta t| = T$, marking the point at which bombardment began. Beyond this point (the shaded area), the TTCF values of unity reflect the presence of a small incoherent scattering background present before bombardment began. The black curves are linear theory predictions resulting from Eq. 10 and a model of the background. The thin dashed line for the top curve is a compressed exponential fit. A clear transition from the linear theory behavior to the compressed exponential dynamics is observed with increasing time T. The data is for a wavenumber range surrounding 0.16 nm^{-1}, corresponding to length scales comparable to the initial ripple wavelength.

using ion flux to scale the stress curvature coefficient obtained for 1 keV Ar$^+$ bombardment of Si by Norris *et al.*[21] would lead to a destabilizing contribution to S_y of roughly -0.03 nm^2/s. Since the observed $S_y(65°)$ = -0.069 nm^2/s is destabilizing, perhaps the stress contribution is higher than simple scaling of the existing Si results would suggest.

IV.   EARLY-TIME DYNAMICS

XPCS enables us to go beyond the study of the early-time kinetics to the examination of the dynamics, though accurately measuring the TTCF in the early regime is challenging because the individual speckle x-ray intensities are much lower than the average intensity used to study the average growth kinetics. However, there is sufficient coherent intensity in these measurements to examine the TTCF near the peak in scattered intensity and cuts through it during the early stages of patterning are shown in Fig. 8. The thick diagonal line is the time horizon at which the difference in time is equal to the total time since bombardment began. This occurs when $|\Delta t| = T$. In dynamical processes, correlations typically exhibit exponential decay (perhaps stretched or compressed) to a baseline, as seen in the top curve, i.e. the latest time T, of the figure. However, at early times, Fig. 8 shows that correlations instead decrease with a nonzero slope to unity at the time horizon. That is, the structure keeps a memory of its early evolution going back to the time that bombardment started. Beyond the time horizon (the shaded area), the TTCF values of unity reflect the presence of a small incoherent scattering background present before bombardment began.

The experimental behavior observed can be compared to theory. Analytic calculation[28] shows that the TTCF

predicted by linear theory is:

$$C_{linear-theory}(q, T, \Delta t) = 1 + \beta(q)\frac{\exp[2R(q)|\Delta t|] - \exp[R(q)(T + |\Delta t|)]}{1 - \exp[R(q)(T + |\Delta t|)]} \tag{10}$$

where $\beta(q)$ is a contrast factor. This assumes that the initial surface state is smooth, which is a good approximation in the present situation. The solid theory lines in Fig. 8 show that, at early times, the lineshapes of the cuts through the TTCF agree well with the theory predictions of Eq. 10. The theory curves use the measured value of $R(q)$ made from fits of the averaged intensity evolution as described above and reflect the effect of an increasing effective contrast due to the increasing fraction of the total scattering that is coming from the surface versus an incoherent background. In particular, the intensity $I(t)$ in the TTCF Eq. 1 is assumed to be the sum of a time-independent background I_0 equal to the initial scattering observed from a smooth surface and the growing sample intensity $I_{sample}(t)$ as calculated from the linear theory fits above. The only additional input for the theory curves in the figure is a single value of the final contrast observable when the background is much smaller than the sample surface scattering. This is taken to be $\beta = 0.165$. Figure 8 shows clearly how the TTCF's evolve from the novel linear theory form predicted by Eq. 10 to a more common compressed exponential lineshape, which is discussed in the next section.

V. LATE-TIME DYNAMICS

In the late-time regime, the TTCF stops evolving on the time scale of the experiment (by ~ 2000 s in the data of Fig. 4) and we consider the stationary intensity auto-correlation function:

$$g_2(q, \Delta t) = \frac{\langle I(q, t')I(q, t' + \Delta t)\rangle}{\langle I(q)\rangle^2} \tag{11}$$

The angular brackets indicate a time averaging over t' and equivalent q values. For both 45° and 65° ion bombardment angles, the $g_2(q, t)$ function is well fit with a compressed exponential Kohlrausch-Williams-Watts (KWW) form[29]:

$$g_2(q, \Delta t) = 1 + \beta(q)\,e^{-2(\frac{\Delta t}{\tau(q)})^{n(q)}} \tag{12}$$

where $\tau(q)$ is the correlation time and $n(q)$ is an exponent greater than or equal to one. The top of Fig. 9a displays the fit values of $n(q)$; the inset shows that a compressed exponential fit better agrees with the data than does a simple exponential form. At low wavenumbers, the KWW exponents are approximately 1.5-1.6. These are comparable to exponents we have found in the nonlinear Kardar-Parisi-Zhang (KPZ) model at low wavenumbers[28] and similar exponents are often reported in a wide range of physical processes[30-35]. These values are also similar to those reported for ion beam nanopatterning of GaSb[12]. Here, however, we see in addition that the KWW exponent systematically decreases to one at high wavenumbers, suggestive of a transition to linear dynamics on short length scales.

The fit correlation times $\tau(q)$ are shown in in the lower part of Fig 9a. There is a low-wavenumber regime with $\tau(q)$ decreasing approximately as q^{-1} and a high wavenumber regime in which $\tau(q)$ decreases approximately as q^{-4}.

In order to better understand the observed late-stage dynamics behavior, we have performed simulations using the 2+1 dimensional anisotropic Kuramoto-Sivashinsky (aKS) equation[36]:

$$\frac{\partial h(\mathbf{r}, t)}{\partial t} = A\,h_y + \nu_x\,h_{xx} + \nu_y\,h_{yy} + \lambda_x\,h_x^2 + \lambda_y\,h_y^2 + \gamma_y\,h_y^3 - \kappa\nabla^4 h + \eta(\mathbf{r}, t) \tag{13}$$

where $\eta(\mathbf{r}, t)$ is a Gaussian white noise and the various coefficients presumably depend on the ion species, energy, and angle of incidence and target material. If they are dominated by sputter yield effects, the nonlinear coefficients can in principle be calculated from knowledge of $Y(\theta)$.[37,38] However, they depend on derivatives up to $\frac{d^3Y}{d\theta^3}$ and, as discussed above, the sputter yield curve for 2 keV Ar^+ on SiO_2 is not so precisely known. Calculations suggest that widely varying values can be obtained from different assumptions about the behavior of $Y(\theta)$. Instead of using calculated nonlinear coefficient values, we have therefore decided to follow the recent simulation study of the aKS equation by Harrison et al.[38] and choose values that yield reasonable behavior. Thus, for simplicity, the simulations were performed with parameters $A = 0.2$, $\nu_y = -0.5$, $\nu_x = 0.5$, $\lambda_x = 2$, $\lambda_y = 2$, $\kappa = 2$ and $\gamma_y = 0$ or $\gamma_y = 2$, as discussed below. The lattice size was 1024×1024. Numerical integrations were performed using the one-step Euler scheme for the temporal discretization with an integration step $dt = 0.01$. The spatial derivatives were calculated by the standard central finite difference discretization method (FDM) on a square lattice with periodic boundary conditions. The surface is taken to be initially flat with uniform random noise on the interval $[-0.1, 0.1]$.

In order to compare experiment and simulation, we equate the simulation ratio of $\sqrt{\frac{\kappa}{|\nu_y|}} = 2$ lattice units with the experimental values $\sqrt{\frac{B}{|S_y|}}$, we find each lattice unit in the simulations to be approximately 2 nm for both irradiation angles 45° and 65°. By equating $|\nu_y|$ and $|S_y|$ for 65°, each simulation time step is approximately 45 seconds. The intensity $I(q)$ has been calculated using the Born/distorted-wave Born Approximation[39] equation:
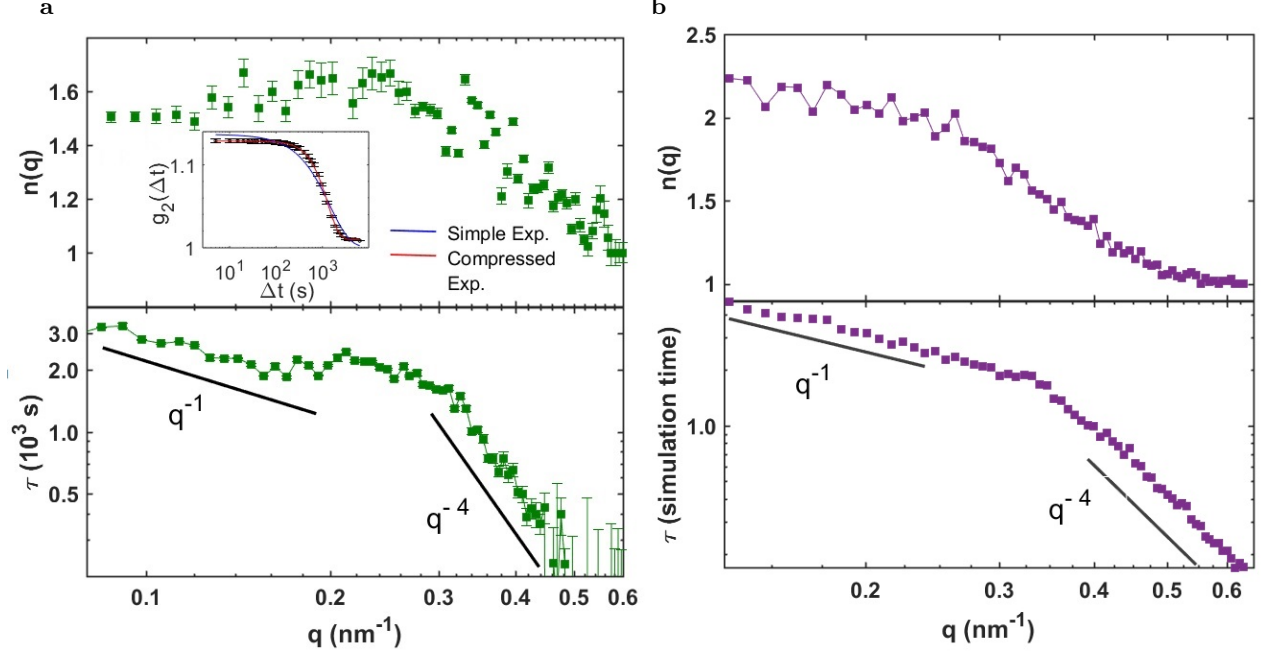

FIG. 9: Compressed exponents $n(q)$ and correlation times $\tau(q)$ during late-stage steady-state dynamics. a) Fit values for experiments with irradiation angle 45°. The inset displays simple and compressed exponential fits to the $g_2(q,t)$ function for $q = 0.24$ nm^{-1}. b) Fit values from simulations of the aKS equation.
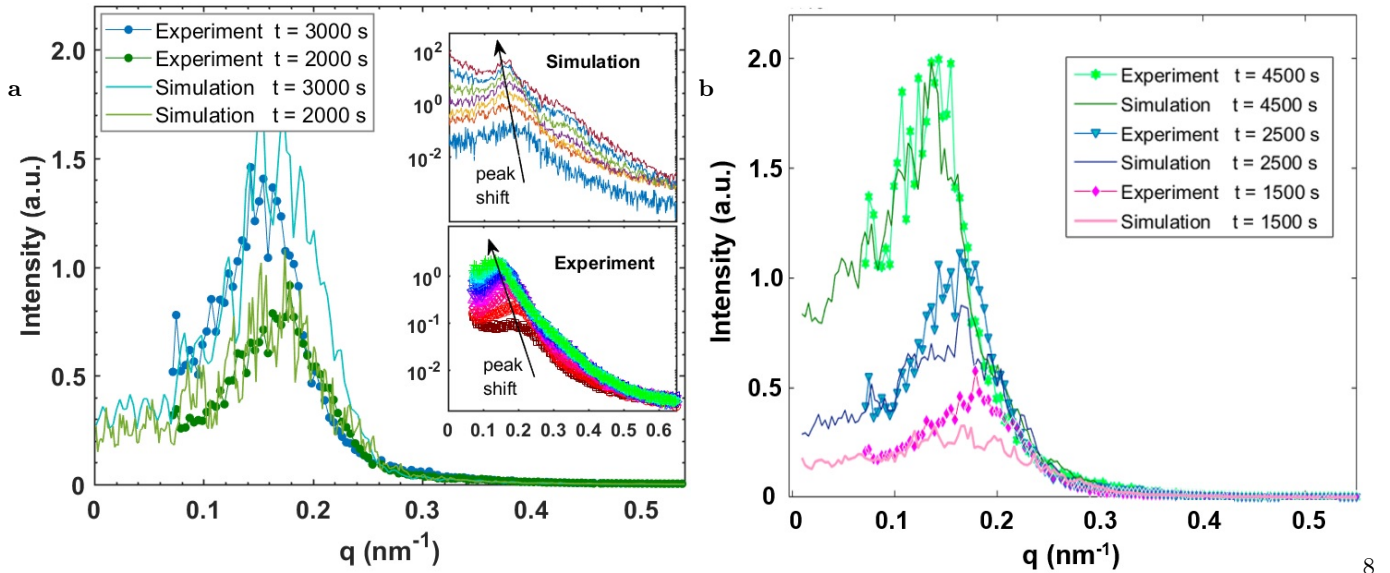

FIG. 10: Comparison of experimental and simulated aKS intensity evolution for bombardment at 65°. a) Comparison with no cubic term in the simulation. The peak shift arrow in the inset displays the evolution in time as the peak of the intensity profile moves to lower values. b) Comparison using a cubic term $\gamma_y = 2$. in the simulation.

$$I(q_x, q_y, q_z) \propto \left| \frac{1}{q_z} \iint dx \; dy \; e^{-iq_z h(x,y)} \; e^{-i(q_x x + q_y y)} \right|^2 \tag{14}$$

where q_z is the z-component of the wave-vector change outside the material in case of Born Approximation or the z-component of the wave-vector change inside the material in case of distorted-wave Born Approximation. In the case of small $q_z h(x,y)$, the intensity $I(q)$ becomes proportional to the height-height structure factor $S(q)$. For simplicity, we have taken $q_z = 1$ in the units of the simulated lattice.

To compare the experimental and simulated kinetics, Fig, 10a exhibits both the speckle-averaged intensity $I(q)$ for the aKS simulation using $\gamma_y = 0$ with the speckle-averaged experimental data for irradiation angle 65°. As can be seen, the experimental results for the early time peak position in the intensity/structure factor matches very well with the aKS equation with the lowest order non-linear term ($\lambda_x h_x^2$ and $\lambda_y h_y^2$); however, the late time experimental data shows a larger coarsening effect that does not match with the simulations. In order to keep pace with the peak shift in the structure factor, third order non-linear terms ($\gamma_y h_y^3$) had to be added to the simulations. Figure 10b shows the $I(q)$ plot for the simulations with $\gamma_y = 2$ and the same other parameters as before. Although the inclusion of the cubic non-linear term with $\gamma_y = 2$ suppresses the value of the intensity peak at early times and also eliminates the secondary peak of the structure factor, the position of the peak matches very well with the experimental data at all irradiation times. This large coarsening effect due to the cubic non-linearities has been studied by Harrison, Pearson and Bradley[37,38]; as they discuss, the term ($\gamma_y h_y^3$) in the aKS equation can originate from an improved approximation for the slope dependence of the sputter yield.

For the late-time dynamics, the intensity autocorrelation function, Eq. 11, has been computed from non-averaged speckle intensities and fit with the KWW form. The top of Fig. 9b shows that the simulations reproduce similar behavior of the KWW exponent as seen in the experiment, namely a value of 1.5-2.2 at low wavenumbers (with the simulated values being somewhat greater than the experimental values) and decreasing toward one at high wavenumbers. Similar behavior is observed in the KPZ model[28], in which the curvature term is stabilizing, rather than destabilizing as here. In both KPZ and the aKS simulations, the high wavenumber behavior of the dynamics can be expected to be dominated by linear terms in the Langevin equations, which would give a KWW exponent of one, as is approached in both simulation and experiment.

The behavior of the aKS simulation correlation times $\tau(q)$ goes from a q^{-1} decrease at low wavenumbers to a much faster q^{-4} decrease at high wavenumbers (bottom of Fig. 9b). This is consistent with nonlinearities dominating the dynamics at low wavenumbers and the linear $\nabla^4 h$ term (physically associated with ion-induced surface viscous flow) dominating the high-wavenumber dynamics. The power-law behaviors of the simulated $\tau(q)$ are in very good agreement with the experimentally observed behavior, suggesting that on SiO_2 there is also a transition to dynamics dominated by a q^{-4} relaxation mechanism, presumably still ion-induced viscous flow even at this late stage of the ripple evolution.

VI. RIPPLE VELOCITY ANALYSIS

Following their self-organized growth, ripples can move across the surface[40]. Depending upon the system, this has been attributed to the slope-dependence of the ion sputter yield or to stress effects. Except for the case of FIB/SEM studies using the specialized case of Ga^+ incident ions[41−45], the only existing measurement of ripple velocity has used fabricated marker grooves with *ex-situ* SEM to examine motion of ripples during 10 keV Xe^+ irradiation of Si[46]. Here we show that surface-sensitive XPCS can be used to examine ripple velocity *in situ* without fabricated markers using a method that should be broadly applicable even at very small wavelengths.

For uniform motion of waves or a uniform flow pattern, homodyne x-ray scattering cannot detect the motion except perhaps due to small edge effects. However, if there is an inhomogeneous flow pattern, interference oscillations can arise in the temporal correlation functions.[47−49] We use this possibility to estimate the surface ripple velocity. When using a focused ion beam which is inhomogeneous along the length of the x-ray footprint on the sample, an oscillatory behavior is observed in the two-time and corresponding $g_2(t)$ correlation functions. As an example, Fig. 11 shows a TTCF and resulting $g_2(t)$ function after the formation of ripples with the focused ion source. Oscillations are present in the correlation functions which are not present during broad beam bombardment. We now proceed to analyze these to determine ripple velocity.

In the presence of a spatially varying velocity field $\mathbf{v}(\mathbf{r})$, the field-field correlation function is[49]:

$$g_1^{ripple}(\mathbf{q}, t) = \frac{1}{\int I(r')dr'} \int I(r) \, e^{i\mathbf{q}\cdot\mathbf{v}(\mathbf{r})t} \, d\mathbf{r} \tag{15}$$

where $I(\mathbf{r})$ is the spatially dependent x-ray intensity. For analysis, we restrict attention to $q = q_0\,\hat{y}$, where q_0 is the wavenumber of the dominant ripples. In the geometry of the experiment here, the key issue is the spread of the x-ray beam footprint along the x-direction because of the grazing-incidence geometry and thus we examine specifically $\mathbf{v}(x)$. We model the incident x-ray beam as a Gaussian with projected standard deviation in the x-direction of $\sigma_{x-ray} = w/\sin\alpha_i \cong 2.2$ mm. The local ripple velocity $\mathbf{v}(x)$ will be in the positive or negative y-direction (i.e. parallel or antiparallel to the projected ion beam on the surface) and will be proportional to the local ion flux $F(x)$:

$$\mathbf{v}(x) = \hat{y}\,v_0\,\frac{F(x)}{F(x_0)} \qquad (16)$$

where v_0 is the maximum velocity, occurring at the center of the ion beam x_0. The shape of the ion flux for a given focusing can be measured through the erosion rate at different points on the sample and will be treated here as approximately Gaussian. With these approximations, and allowing the ion beam center to be potentially offset from the x-ray beam center by a distance x_0, the field-field correlation function is:

$$g_1^{ripple}(\mathbf{q},t) = \frac{1}{\sqrt{2\pi}\,\sigma_{x-ray}} \int e^{\frac{-x^2}{2\,\sigma_{x-ray}^2}}\, exp\left[iq_0\,v_0\,t\,e^{\frac{-(x-x_0)^2}{2\sigma_{ion}^2}}\right]dx \qquad (17)$$

This function is evaluated numerically. In addition to evolution of the nonuniform ripple pattern, there will be evolution of other surface features during bombardment. If the two are uncorrelated, the total field-field correlation function is:

$$g_1^{total}(t) = g_1^{non-ripple}(t) + g_1^{ripple}(t) \qquad (18)$$

As shown above, the component of the correlation not associated with ripple propagation $g_1^{non-ripple}(t)$ can be modeled with a compressed exponential decay. From the equations above, the homodyne $g_2(t)$ can then be calculated from the Siegert relation $g_2(q,t) = 1 + |g_1(q,t)|^2$. We use a reasonable value of $\sigma_{ion} = 2$ mm for the given focus condition and $x_0 = 0$. The final results are not highly sensitive to the exact values of these parameters. Figure 11b shows the result of a fit to the experimentally observed $g_2(t)$, from which we obtain a maximum ripple velocity of $v_0 \approx 0.28$ nm/s. Note that the homodyne correlation functions are sensitive to the variation in ripple velocity, not the ripple velocity itself. However, in this case the velocity is proportional to the ion flux and we can well model and measure that flux, so that an estimate of velocity itself is obtained. Calculations using slightly different parameters for the X-ray and ion beam sizes and offset suggest that the resulting uncertainty on v_0 is of the order of 20%.

If ripple motion is driven by sputter erosion, then the velocity of ripples is[1,40]:

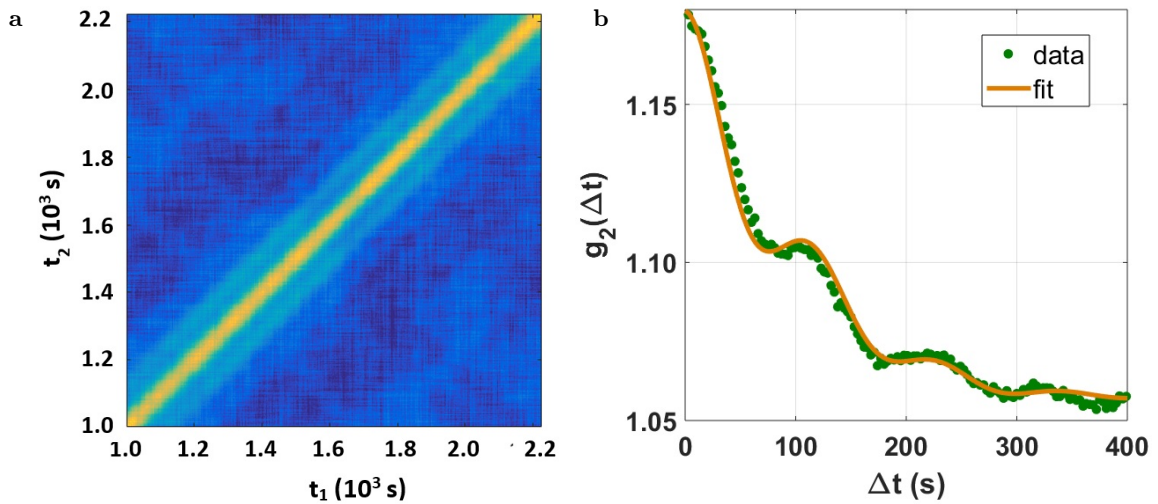$$v(\theta) = -\frac{F}{n}[cos\theta\frac{dY(\theta)}{d\theta} - Y(\theta)sin\theta] \qquad (19)$$

FIG. 11: Oscillations in the XPCS correlation functions due to ripple motion during ion bombardment with an inhomogeneous ion beam. a) Late-time TTCF at $q = 0.11$ nm^{-1}. b) Resulting $g_2(\Delta t)$ function with fit curve based on ripple velocity model described in text.
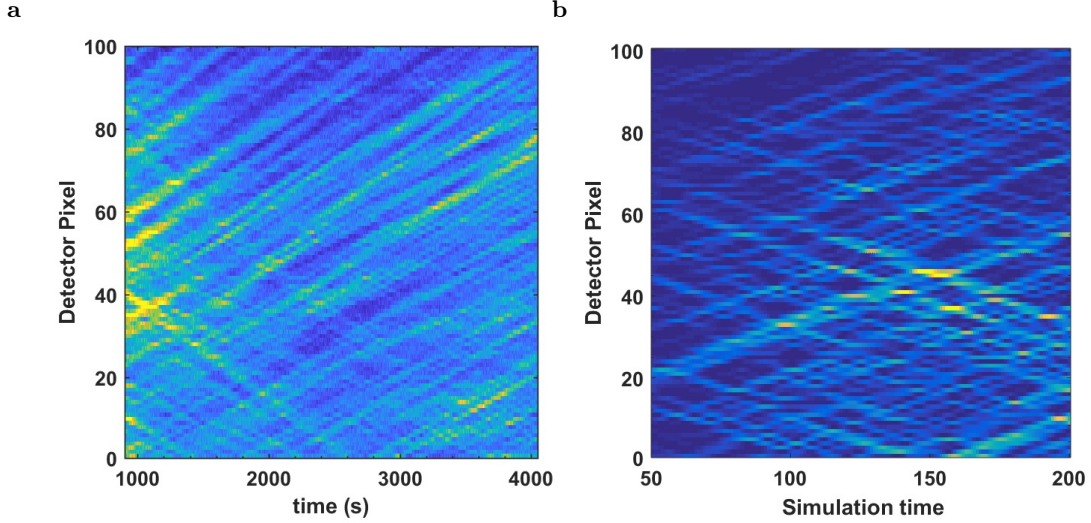
FIG. 12: "Waterfall" plots showing how speckles move with time during ripple motion across the surface. a) Observed speckle motion during 45°bombardment at $q = 0.11$ nm^{-1} when using a focused ion beam. b) Speckle motion from simulation using the aKS equation with a linear triangular velocity gradient function.

where F is the ion flux and n is the atomic number density. Using sputter yield values entirely from SRIM, this gives a theoretical ripple velocity essentially equal to the value of 0.28 nm/s found experimentally from analysis of the TTCF in the manuscript. However, as noted above, for 2 keV Ar$^+$ bombardment of SiO$_2$, there is some uncertainty about the sputter yield and its variation with angle. Use of the Yamamura et $al.$ sputter yield angular dependence calculated with known angular parameters for Si gives near cancellation of the two terms in Eq. 19, resulting in a theoretical prediction that is an order of magnitude smaller. Recently, Kumar et $al.$[19] have used sputter yield values from the SDTrimSP package, which is closely related to SRIM, to estimate a ripple velocity of $v \approx 0.1$ nm/$(10^{15}$ ions/cm$^2)$ for 45° bombardment with 500 eV Ar$^+$ ions. Without worrying for a moment about the difference in ion energies, for the ion flux of 3×10^{14} used for 45° bombardment here, this gives a ripple velocity of approximately 0.033 nm/s, which is much smaller than the measured value in this work. However the factor of four increase in ion energy for the experiments here could potentially account for the difference. Clearly better measurements of the sputter yield are necessary to assess the level of quantitative agreement that theory makes with the experimental measurement.

In addition to creating oscillations in the correlation functions, inhomogeneous velocities also cause movement of speckles themselves. For a uniform gradient of velocity in a flow pattern:

$$\mathbf{v}(r) = \mathbf{v}_0(r) + \mathbf{\Gamma} \cdot \mathbf{r} \tag{20}$$

with $\mathbf{\Gamma}$ being the velocity gradient tensor, Fuller et $al.$ showed that the speckles move in reciprocal space as[47]:

$$\frac{d\mathbf{q}}{dt} = -\mathbf{\Gamma^T} \cdot \mathbf{q} \tag{21}$$

For the case of ripples moving in the $\pm\hat{y}$ direction with a velocity gradient in the x-direction, this leads to speckle motion in the q_x direction with velocity $\frac{dq_x}{dt} = \pm\Gamma q_0$, where q_0 is the ripple wavenumber.

In the GISAXS geometry, speckle motion in the q_x-direction would appear primarily as the vertical movement of speckles on the detector. For the experiments reported here, the inhomogeneous ripple velocity is not a uniform gradient; instead, the x-ray footprint straddles the position of peak ion beam intensity so that the ripple velocity has regions in which it is increasing with increasing x-position and regions in which it is decreasing. Based on this analysis, when bombarding the surface with a highly focused ion beam, we therefore expect speckle motion to be observed in the vertical direction on the detector, moving both up and down,. This is indeed observed as shown in the "waterfall" plot of Fig. 12a. Using the slope of speckle motion in Fig. 12a, the value of Γ can be estimated from $\frac{dq_x}{dt} = \frac{\Delta q_x}{\Delta(pixel_Y)} \times slope$. This leads us to a velocity gradient of $\Delta v = \Gamma \cdot \Delta r \approx 0.36$ nm/s between two positions $\Delta r = 2\,mm$ apart. This is reasonable compared to the peak velocity derived above and the spread in ion intensity on focusing.

There are two potential complications to this analysis. First, with an inhomogeneous ion beam, there will also be speckle motion due to the gradient in erosion rate $\Delta = \delta v_{erosion}/\delta x$; this would lead to a speckle velocity $q_z\Delta$. However no consistent variation in speckle velocity with q_z is observed, so we assume that this effect is not sufficiently

large to affect the results. A second potential complication in this analysis of speckle motion is that, since there is some coarsening of the ripples during bombardment, the inhomogeneous ion beam will lead to a variation in both ripple speed and ripple wavelength. However simulations show that spatial variation of the A coefficient in the aKS equation, which drives ripple motion, is necessary and sufficient to cause speckle motion such as observed in the experiment. Figure 12b shows the speckle motion from simulation on a 4096×512 lattice using the aKS equation with a triangle-shaped dependence of A on position x, increasing linearly for half of the lattice and decreasing lineary for the other half. This shape is motivated by the x-ray footprint straddling the peak of the ion flux. Thus the simulations results provide strong evidence that it is inhomogeneous ripple motion causing the experimentally observed speckle motion rather than inhomogeneous ripple wavelength.

VII.   CONCLUSION AND PERSPECTIVE

Surface-sensitive coherent x-ray scattering has provided here a detailed new view of the evolving relationship between kinetics and dynamics on a surface undergoing self-organized nanopatterning. At length scales comparable to the initial ripple wavelength, the early stage correlations show that not only the average ripple growth, but also the underlying dynamics, can be understood within the framework of linear stability theory. Due to the simple exponential growth of fluctuations occuring in this regime, the surface exhibits a novel correlation behavior with memory stretching back to the beginning of bombardment. Fitting the wavenumber-dependent amplification factor requires the full wavenumber dependence of the Orchard viscous relaxation term. Moreover, the fit parameters coming from the Orchard term are in good agreement with SRIM simulation and published estimates. For 45 ° bombardment, the magnitude of the amplification factor is consistent with erosive effects dominating the surface evolution at low wavenumbers, while at 65 ° bombardment, it appears that some other mechanism, perhaps stress, is needed.

Interestingly, for length scales comparable to the ripples, the characteristic time for the growth of fluctuations is $\tau(q) = 1/2R(q) = 100$ s. It's seen in Fig. 8 that the time Δt over which strong surface correlations persist does not grow significantly beyond this value. Instead the dynamics transitions away from linear theory behavior at about this time. Thus the characteristic time defined by the amplification factor is also closely related to the transition *away* from linear stability theory dynamics. In the late stages of patterning, the underlying surface dynamics as measured by the TTCF reaches a steady state. The saturation of the correlation time observed here makes an interesting contrast with the case of normal-incidence ion beam nanopatterning of dots on GaSb, for which Bikondoa *et al.*[12] observed a continuous increase in correlation time throughout their experiment. Since simple models of nanopatterning exhibit only a low-wavenumber instability producing poorly ordered surfaces, the case of GaSb may be more complex than that of SiO_2.

In the late stages, the long length-scale dynamics is driven by nonlinearities, producing a compressed exponential decay of the $g_2(t)$ autocorrelation function. In this regime, surface fluctuations persist with a decay time decreasing as q^{-1}. However on short length-scales the dynamics appears to remain linear, and is consistent with ion-enhanced viscous surface relaxation, as observed in the early stages. Simulations of the aKS equation reproduce this behavior well.

The nanoscale *dynamical* information about surface memory and ripple motion provided here by coherent x-ray scattering provides the possibility of a paradigm shift away from thinking only in terms of average *kinetics*. Increasing coherent x-ray flux from new and upgraded sources will significantly enhance further applications of surface-sensitive coherent scattering to investigate ion beam nanopatterning. The coherent flux available for the present experiments limited the early-stage dynamics investigations to length scales comparable to the ripple wavelength and in the late stage did not allow the full observation of the presumed transition to linear behavior with increasing wavenumber. However, our recent real-time "non-coherent" x-ray studies of ion beam nanopatterning of Si have pointed out the importance of examining higher wavenumber (i.e. shortor length-scale) behavior to distinguish between competing theories of surface mechanisms driving patterning[21]. Such studies of dynamics on length scales 2-3 times shorter should soon be possible. Interestingly, at the relatively long length scales studied here, the coherent contrast β does not decrease significantly when the ion beam is turned on, showing that there is no "missing" dynamics happening on faster time scales. Nonetheless, picosecond-scale dynamics must exist on the length scale of the ion collision cascade itself – approximately 1 nm. These would be quite revealing to examine if sufficient flux becomes available from free-electron laser sources.

VIII.   ACKNOWLEDGMENTS

IX. REFERENCES

1. R.M. Bradley and J.M.E. Harper, *J. Vac. Sci. Technol. A* **6**, 2390 (1988).
2. S. Facsko, T. Dekorsy, C. Koerdt, C. Trappe, H. Kurz, A. Vogt, and H.L. Hartnagel, *Science* **285**, 5433 (1999).
3. H. Zhou, L. Zhou, G. Ozaydin, K.F. Ludwig Jr. and R.L. Headrick, *Phys. Rev. B* **78**, 165404 (2008).
4. G. Carter and V. Vishnyakov, *Phys. Rev. B* **54**, 17647 (1996).
5. S. Facsko, T. Bobek, A. Stahl, H. Kurz and T. Dekorsy, *Phys. Rev. B* **69**, 153412 (2004).
6. C.S. Madi, E. Anzenberg, K.F. Ludwig, Jr. and M.J. Aziz, *Phys. Rev. Lett.* **106**, 066101 (2011).
7. S.A. Norris., J. Samela., L. Bukonte, M. Backman, F. Djurabekova, K. Nordlund, C.S. Madi, M.P. Brenner and M.J. Aziz, *Nature Communications* **2**, 276 (2011).
8. M.P. Harrison and R.M. Bradley, *Phys. Rev. B* **89**, 245401 (2014).
9. M. Castro, R. Gago, L. Vazquez, J. Muñoz-Garcia and R. Cuerno, *Phys. Rev. B* **86**, 214107 (2012).
10. S.A. Norris, *Phys. Rev. B* **86**, 235405 (2012).
11. O. Bikondoa, D. Carbone, V. Chamard and T.H. Metzger, *J. Phys.-Cond. Matt.* **24**, 445006 (2012).
12. O. Bikondoa, D. Carbone, V. Chamard and T.H. Metzger, *Scientific Reports* **3**, 1850 (2013).
13. M.G. Rainville, C. Wagenbach, J.G. Ulbrandt, S. Narayanan, A.R. Sandy, H. Zhou, R.L. Headrick and K.F. Ludwig, Jr., *Phys. Rev. B* **92**, 214102 (2015).
14. J.G. Ulbrandt, M.G. Rainville, C. Hoskin, S. Narayanan, A.R. Sandy, H. Zhou, K.F. Ludwig, Jr. and R.L. Headrick, *Nature Physics* **12**, 794 (2016).
15. G. Ju, D. Xu, M.J. Highland, C. Thompson, H. Zhou, J.A. Eastman, P.H. Fuoss, P. Zapol, H. Kim and G.B. Stephenson, *Nature Physics* https://doi.org/10.1038/s41567-019-0448-1 (2019).
16. M. Sutton, S.G.J. Mochrie, T. Greytak, S.E. Nagler, L.E. Berman, G.A. Held and G.B. Stephenson, *Nature* **352**, 608 (1991).
17. M. Sutton, *Comptes Rendus Physique* **9**, 657 (2008).
18. C.C. Umbach, R.L. Headrick and K.-C. Chang, *Phys. Rev. Lett.*, **87**, 246104 (2001).
19. M. Kumar, D.P. Datta, T. Basu, S.K. Garg, H. Hofsäss and T. Som, *J. Phys.: Condens. Matter* **30**, 334001 (2018).
20. A. Keller, S. Facsko and W. Möller, *J. Phys.: Condens. Matter* **21**, 495305 (2009).
21. S. Norris, J. Perkinson, M. Mokhtarzadeh, E. Anzenberg, M.J. Aziz and Ludwig, *Scientific Reports* **7**, 2016 (2017).
22. S.E. Orchard, *Appl. Sci. Res.* **11A**, 451 (1962).
23. R.M. Bradley, *Phys. Rev. B* **84**, 075413 (2011).
24. The Stopping and Range of Ions in Matter (SRIM): SRIM 2013 available free from http://www.srim.org/SRIM/SRIM2011.htm.
25. M.P. Seah and T.S. Nunney, *J. Phys. D: Appl. Phys.* **43**, 253001 (2010).
26. M.P. Seah, C.A. Clifford, F.M.Green and I.S. Gilmore, *Surf. Interface Anal.* **37**, 444 (2005).
27. Y. Yamamura, Y. Itikawa and N. Itoh, *Institute of Plasma Physics Report* IPP-A-26, Nagoya University, (1983).
28. M. Mokhtarzadeh and K. Ludwig, *J. Synchrotron Rad.* **24**, 1187 (2017). Note that the sign convention for $R(q)$ in this reference is the opposite to that used in the present paper.
29. G. Williams and D.C. Watts, *Trans. Faraday Soc.* **66**, 80 (1970).
30. K. Wong, R.P. Krishnan, E.M. Dufresne, K. Ohara, A.r. Sandy and S. Chathoth, *Acta Materialia* **155**, 35 (2018).
31. J.L. Harden, H. Guo, M. Bertrand, T.N. Shendruk, S. Ramakrishnan and R.L. Leheny, *J. Chem. Phys.* **148**, 044902 (2018).
32. H. Conrad, F. Lehmkühler, B. Fischer, F. Westermeier, M.A. Schroer, Y. Chushkin, C. Gutt, M. Sprung and G. Grübel, *Phys. Rev. E* **91**, 042309 (2015).
33. R.L. Leheny, *Current Opinion in Colloid & Interface Science* **17**, 3 (2012).
34. A. Madsen, R.L. Leheny, G. Guo, M. Sprung and O. Czakkel, *New J. Phys.* **12**, 055001 (2010).
35. L. Cipelletti, L. Ramos, S. Manley, E. Pitard, D.A. Weitz, E.E. Pashkovski and M. Johansson, *Faraday Discuss.* **123**, 237 (2003).
36. M. Rost and J. Krug, *Phys. Rev. Lett.* **75**, 3894 (1995).
37. D.A. Pearson and R.M. Bradley, *J. Phys.: Condens. Matter* **27** 015010 (2015).
38. M.P. Harrison, D.A. Pearson and R.M. Bradley, *Phys. Rev. E* **96**, 032804 (2017).

39. S.K. Sinha, E.B. Sirota, S. Garoff and H.B. Stanley, *Phys. Rev. B* **38**, 2297 (1988).

40. P.F.A. Alkemade, *Phys. Rev. Lett.* **96**, 107602 (2006).

41. S. Habenicht, K.P. Lieb, J. Koch and A.D. Wieck, *Phys. Rev. B* **65**, 115327 (2002).

42. Q. Wei, J. Lian, L.A. Boatner, L.M. Wang and R.C. Ewing, *Phys. Rev. B* **80**, 085413 (2009).

43. W.J. Moberly Chan, *J. Phys.: Condens. Matter* **21**, 224013 (2009).

44. H. Gnaser, B. Reuscher and A. Zeuner, *Nucl. Instrum. Methods Phys. Res., Sect. B* **285**, 142 (2012).

45. D. Kramczynski, B. Reuscher, and H. Gnaser, *Phys. Rev. B* **89**, 205422 (2014).

46. H. Hofsäss, K. Zhang, H.G. Gehrke and C. Brüsewitz, *Phys. Rev. B* **88**, 075426 (2013).

47. G.G. Fuller, J.M. Rallison, R.L. Schmidt and L.G. Leal, *J. Fluid Mech.* **100**, 555 (1980).

48. A. Fluerasu, A. Moussaid, P. Falus, H. Gleyzolle and A. Madsen, *J. Synchrotron Radiat.* **15**, 378 (2008).

49. R. Lhermitte, M.C. Rogers, S. Manet and M. Sutton, *Rev. Sci. Instrum.* **88**, 015112 (2017).

---

* Electronic address: `ludwig@bu.edu`; Corresponding author